Accepted Manuscript

Crack path simulation in a particle-toughened interlayer within a polymer composite Laminate

G. Borstnar, M.N. Mavrogordato, Q.D. Yang, I. Sinclair, S.M. Spearing

PII: S0266-3538(16)30805-3

DOI: 10.1016/j.compscitech.2016.07.024

Reference: CSTE 6470

To appear in: *Composites Science and Technology*

Received Date: 28 January 2016

Revised Date: 20 July 2016

Accepted Date: 24 July 2016

Please cite this article as: Borstnar G, Mavrogordato MN, Yang QD, Sinclair I, Spearing SM, Crack path simulation in a particle-toughened interlayer within a polymer composite laminate, *Composites Science and Technology* (2016), doi: 10.1016/j.compscitech.2016.07.024.

Crack path simulation in a particle-toughened interlayer within a polymer composite laminate

G. Borstnar[1,*], M. N. Mavrogordato[1], Q. D. Yang[2], I. Sinclair[1] and S. M. Spearing[1]
[1] Faculty of Engineering and the Environment, University of Southampton, Highfield, Southampton SO17 1BJ, UK
Email*: gb1a15@soton.ac.uk
[2] Department of Mechanical and Aerospace Engineering, University of Miami, Coral Gables, FL 33124, USA

Keywords: A - Polymer matrix composites (PMCs); C - Finite element analysis (FEA); C - Crack; D - Non-destructive testing; Augmented Finite Element Method

Abstract

With recent advances in computational resources and the development of arbitrary cracking methods, such as the Augmented Finite Element Method (A-FEM), more complex simulations can now be represented featuring multiple interacting cracks. It has been established that Mode I crack propagation in particle-toughened interlayers within some toughened Carbon Fibre Reinforced Polymer (CFRP) laminates involves a discontinuous process zone, rather than a distinct crack tip. This results from multiple cracks forming ahead of the main crack that subsequently coalesce, leaving behind bridging ligaments that may then provide traction across the crack flanks. An idealised two-dimensional A-FEM model is presented in this work, which represents the 'particles' as one-dimensional cohesive regions. The model shows that variables such as particle spacing, distribution, strength and toughness, and fibre interface strength can be tailored in order to maintain the crack path within the interlayer. This competition between crack paths is important, as a reduction in composite toughness is reported when the crack path migrates to the fibre interface. The simulations are complemented by time-resolved Synchrotron Radiation Computed Tomography (SRCT) data, which identify the chronology of the damage processes, along with the effects of particle distribution on the crack path and the formation of bridging ligaments.

1 INTRODUCTION

The use of Carbon Fibre Reinforced Polymers (CFRPs) in primary aerospace structures is increasing. However, low velocity impacts that may occur in service can lead to a substantial loss in mechanical properties without noticeable surface damage [1]. An effective strategy to reduce the spread of delaminations caused by impacts is to disperse secondary phase particles within the interlaminar regions in order to toughen the interlayer [2-6]. However, there remains uncertainty in precisely how this added toughness arises, due to a partial micromechanical understanding of interlaminar fracture processes. In bulk particle-toughened resins, toughening mechanisms such as; crack path deflection [7,8], crack pinning [7], particle bridging [9], localised shear yielding [10], and particle/resin de-bonding and subsequent void growth [11] have been identified. However, it has been established that bulk resin toughness does not translate directly into composite interlaminar toughness [12]. This discrepancy has been attributed to the constraint of the surrounding plies [6,13]. The crack path may also propagate along or inside the ply, since additional fibre interfaces offer an alternative crack path [14], [15]. Previous work has shown that in particle-toughened interlayers, particles that de-bond ahead of the 'crack tip' are able to draw the crack path away from the fibre interface, enabling the development of a more tortuous ligament-rich crack path [16]. Other authors have suggested that in similar,

micron-scale particle-toughening systems, smaller particles (~10 μm in diameter) with a uniform distribution will result in a higher interlaminar fracture toughness than larger particles with a poor distribution [17]. However, it is far from clear as to which combination of parameters results in an optimal micro-structure to increase macro-scale toughness.

In this work, the new Augmented-Finite Element Method (A-FEM) [18] has been implemented, which was developed further by Gu *et al.* to better handle unstable crack initiation and propagation [19]. This is classed as an arbitrary crack path method (grounded on the seminal Partition of Unity (PoU) theory [20]) that can initiate and propagate cracks without *a priori* knowledge, which have been shown to be relatively mesh independent [18,21,22]. A 2D plane strain model is used to simulate Mode I interlaminar crack propagation, wherein idealised 'particles' are represented by one-dimensional (1D) segments. The resin, fibre interface and particle properties were defined in the A-FEM subroutine (implemented in ABAQUS FEA 6.12-1 (Dassault Systemes, Velizy-Villacoublay, France)) with a bilinear cohesive law. Previously, Matous *et al.* modelled a heterogeneous interlayer and coupled the micro- and meso-scales through a multi-scale cohesive model, incorporating circular particles with different stiffnesses, sizes, and volume fractions [23]. However, the idealised model in the present work directly interrogates the relative strengths of the resin, particles, and the fibre interface; which is the key competing crack path. The parametric study identified parameters that influence crack migration from the interlayer to the fibre interface. A weaker fibre interface, lower particle volume fraction (V_F), larger particle spacing and higher particle strength facilitated this migration. The work is supported with time-resolved Synchrotron Radiation Computed Tomography (SRCT) data, whereby the chronology of the damage evolution and the influence of local particle distribution could be compared to the model.

2 MATERIALS AND METHODS

Developmental and proprietary CFRPs were prepared by Cytec Industries, and manufactured and cured following a standard aerospace autoclave cycle. Panels consisted of a 16-ply uni-directional layup, with a 10 mm wide, 40 μm thick, polytetraflouroethylene (PTFE) insert placed at mid-plane in order to control the initiation of fracture. 150 mm long specimens were cut to give a 2.5 x 3 mm cross-section, providing a relatively uniform X-ray path throughout the specimen rotation. Secondary phase particles were dispersed in the interlayer at a volume fraction, v_f of 13 %, consistent between the materials, with a post-cure v_f of about 40-50 %. The base resin and proprietary intermediate modulus carbon fibre also remained consistent. Two different types of thermoplastic particle were used: Material A (Mat. A) featured particles with a tendency for de-bonding ahead of the crack tip, with sizes ranging between 5 – 30 μm: Material B (Mat. B) contained particles about 10 μm in diameter, which tend to both crack internally and bridge the crack flanks. Mode I initiation fracture toughness is normalized as 0.8 to 1, for Mat. A to Mat. B respectively.

Specimens were loaded into an *in situ* loading device, which drove a wedge into the mid-plane of the CFRP causing Mode I opening of the crack. An initial loading step grew the crack about 5 mm from the edge of the insert, after which the specimen was scanned. The specimen was then subsequently loaded in order to capture Mode I

crack propagation in 3D in a time-resolved manner. The CT slices presented are located away from the free-edges and in the middle of the sample. The SRCT experiments were conducted at the Swiss Light Source on the TOMCAT beamline at the Paul Scherrer Insitut, Villigen, Switzerland. Scans were conducted at a voxel resolution of 0.325 μm , with a detector size of 2560 x 2160 pixels. A beam energy of 15 kV was used, with 1501 projections taken at an exposure of 150 ms for the 180-degree rotation. A propagation distance of 23 mm was used to better distinguish the edges between materials of similar attenuation via phase-enhanced contrast [24]. The CT data was reconstructed using the in-house GRIDREC method [25].

3 NUMERICAL SIMULATION

3.1 – Augmented Finite Element Method

2D A-FEM elements developed by Gu et al. [19] have been used because they can account for multiple arbitrary intra-element cracks and their interactions. This is achieved through the introduction of internal node pairs with displacements as internal nodal degrees of freedom, which are later condensed at the elemental level [18,19]. Crack initiation and propagation can be simulated, whereby the initiation criteria and subsequent forces on the crack flanks during separation are defined by a cohesive law. Significant for this work is that multiple intra-element cracks can be accounted for, since the augmentation procedure can be repeated on the same element. This allows for bifurcating and coalescing cracks to be accounted for, which is critical in simulating the discontinuous damage observed in the particle-toughened CFRPs presented in this work.

3.2 – Model implementation

The model uses both standard elastic elements (CPS4) and A-FEM elements. The elastic elements define the neighbouring ply properties, and the ‘crackable’ A-FEM elements define the resin, fibre interfaces and the particle properties (described in Section 3.3). Figure 1 illustrates the 2-D model, where an initial starter crack is used to bring the crack towards the region of interest (ROI). Within this region, 1-D segments define the particles and the fibre interfaces. The thickness of the interlayer is consistent with the ~30 μm interlayers seen in the CT data, and the displacement controlled loading conditions were applied 0.33 mm (more than 10x an interlayer thickness) away from the start of the ROI to simulate the Mode I loading. The output of the model determines the location along the ROI where the bottom fibre interface elements fail. This position is expressed as a percentage of the total ROI length, which is labelled in the plots as ‘% of interlaminar failure’.

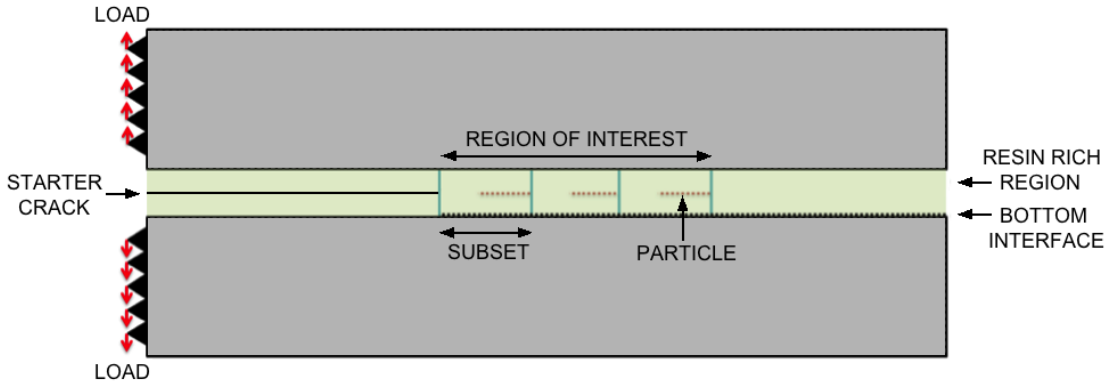

Figure 1: Illustration of the interlayer model and the region of interest containing 1-D particles in each subset (not to scale)

One of the main concerns with using arbitrary crack path methods is whether the mesh is sufficiently refined. An analytical estimate of element size (described in [26]) for a crack in an infinite body was used as an initial starting point, since properties at these length scales are not well established. The characteristic length (l_c) was estimated as 12 μm, using $l_c = \frac{G_{IC} \times E}{\hat{\sigma}^2}$ [26], where the elastic modulus (E) was 3000 MPa, Mode I toughness (G_{IC}) was 0.01 mJ/mm^2, and the peak stress ($\hat{\sigma}$) was 50 MPa. The mesh sensitivity study was conducted using smaller elements from 6 μm to 1.4 μm, which provided between 5 and 21 elements across the interlayer thickness to give better control over local microstructure. It was determined that the crack paths were insensitive for element sizes that were 2.7 μm and below. The 2.7 μm mesh size was chosen because it produced a crack path consistent with finer meshes and at an acceptable computational cost.

3.3 – Key properties and variables

Currently, there is limited information regarding suitable cohesive parameters to define resin and fibre interface properties at these length-scales, therefore the current model aims to identify trends with parametric variation in the relative properties between the resin, fibre interface and particles, as well as particle size and distribution. In the first instance, the Mode I and Mode II cohesive strengths were assumed to be equal. The baseline properties were chosen as follows: the neat resin and top fibre interface toughness was 0.125 mJ/mm^2, with a critical strength of 50 MPa; the particles, fibre interfaces and resin moduli were 3 GPa; and the surrounding plies were assigned isotropic properties with a Young's modulus of 150 GPa. These properties and the cohesive law shape parameter (λ= 3 x10^{-4}) were kept consistent throughout the simulations. Figure 2(a) illustrates the key variables that were investigated in the presented work, wherein the simulations determined which properties influence the crack path. Figure 2(b) shows an example of the crack path merging with the fibre interface. Figure 3 shows the linear particle distributions that were investigated, which will be referred to in the text along with the model numbers summarised in Table 1.

Table 1: Key model properties and variables

Model No.	Particle					Fibre interface	
	$\hat{\sigma}$ [MPa]	$G_{I/II\,C}$ [mJ/mm^2]	Spacing [μm]	Size [μm]	Prox. [μm]	$\hat{\sigma}$ [MPa]	$G_{I/II\,C}$ [mJ/mm^2]
1	0	0	13.5-29.7	13.5-29.7	13.5	30-40	0.0075-0.01
2	1-50	0.01-0.08	27	27	13.5	40	0.01
3	30-50	0.02	5.4-40.5	5.4-40.5	13.5	40	0.01
4	30-50	0.02	5.4-40.5	5.4-40.5	13.5	35	0.01
5	30	0.02	2.7-24.3	8.1-24.3	13.5	35	0.01
6	30	0.02	2.7-24.3	24.3	13.5-2.7	35	0.01

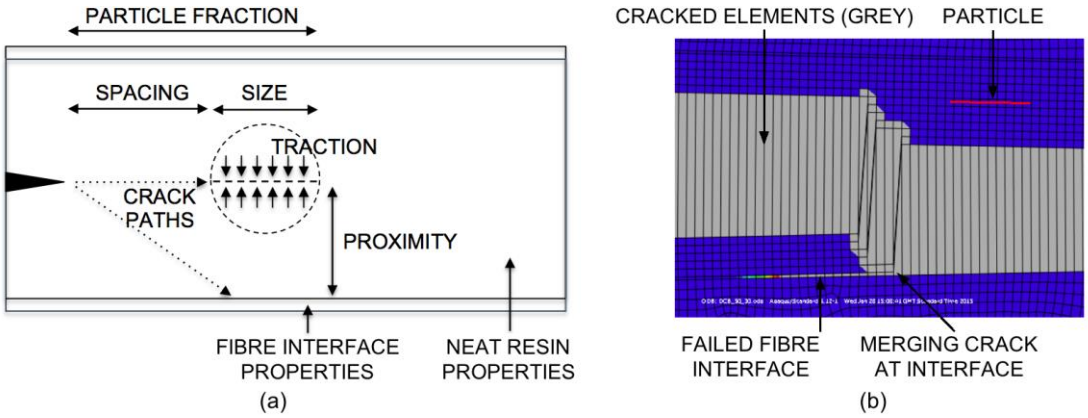

Figure 2: Showing (a) a schematic of the key variables and potential crack paths, and (b) an example of a crack path merging at the fibre interface.

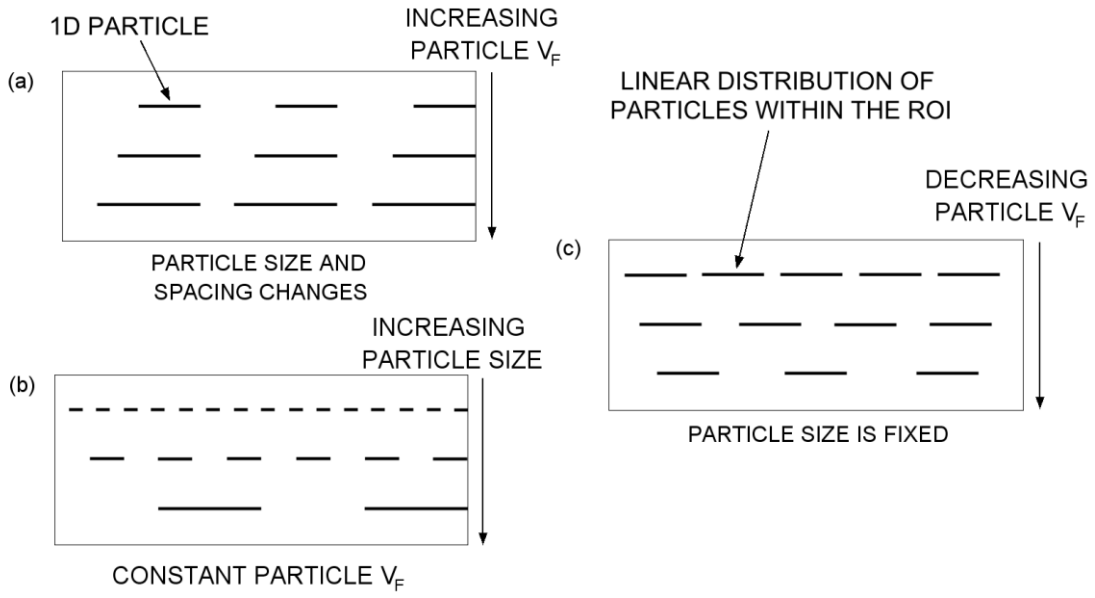

Figure 3: Schematic of the key variations in the 1-D particle distribution along the ROI, with each row showing: (a) an increase in linear particle v_f, maintaining the same number of particles: (b) an increasing particle size/spacing at a constant v_f: and (c) an increased particle spacing with the consequent reduction in particle v_f

4 RESULTS

4.1 – Particle distribution effects captured with SRCT

Figure 4 shows two load steps captured experimentally in two separate locations in the Mat. A specimen, with the corresponding post-growth slice placed below the pre-growth slice. Figure 4(a) shows the effects of a large (i) particle-depleted region, where an absence of de-bonding particles appears to have triggered failure at the fibre interface. The smooth appearance of the failure at the fibre interface can be compared to the ligament-rich crack in the wake, where numerous (ii) small resin strands and (iii) larger ligaments form, which provide tractions across the crack flanks. The chronology of the process is also established, whereby the fibre interface fails while the crack path is still in the interlayer, rather than by a singular crack tip propagating

towards the fibres. On the right hand side of the image, the particle appears to have de-bonded significantly, indicating that the particles within the failure process zone may have the ability to 'draw' the crack path back into the toughened interlayer. Figure 4(b) shows the effects of a (iv) smaller particle-depleted region, where the crack has propagated through the neat resin towards the particles ahead of it. This suggests that there is a critical size of particle-depleted region that may facilitate failure at the fibre interface.

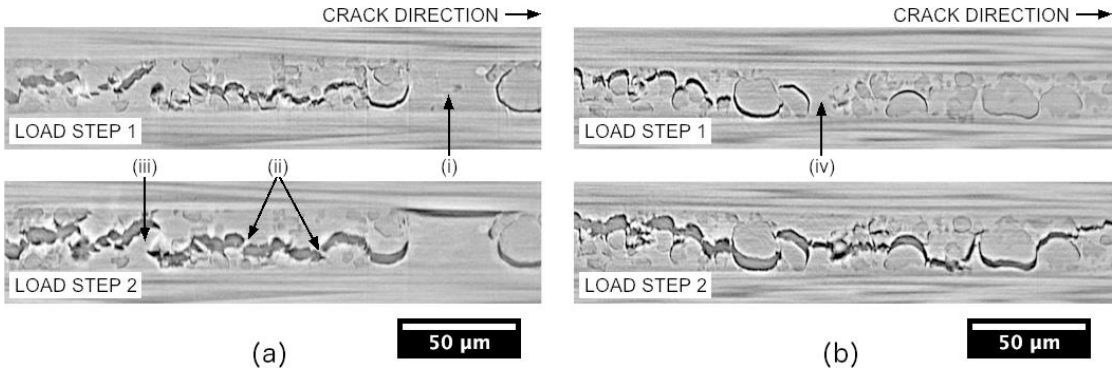

Figure 4: SRCT slices of Mat. A, with the crack going from left to right showing, (a) a large particle-depleted region where failure is tripped at the fibre-interface, and (b) a smaller particle-depleted region where the crack path crosses the neat resin

4.2 – Proportion of de-bonded particles

In this study, three particles were simulated as traction-free discontinuities in the ROI with lower fibre interface strengths of 0.6, 0.7 and 0.8 relative to the neat resin (as defined by Model 1 in Table 1). Given that such de-bonds in Mat. A occur far ahead of the crack tip (Figure 4), their contribution to toughness is assumed to be negligible in this first simulation. The linear particle v_f was changed from 25 % to 55 %, as shown in Figure 3(a), creating particle separation distances up to the order of an interlayer thickness. Figure 5(a) shows that as the fraction of de-bonded particles is decreased (*i.e.* larger particle-depleted regions) the fibre interface becomes more likely to fail, consistent with the CT observation of local particle-depleted regions in Figure 4(a). The graph also shows failure through the interlayer is promoted by a stronger fibre interface, which is the competing crack path.

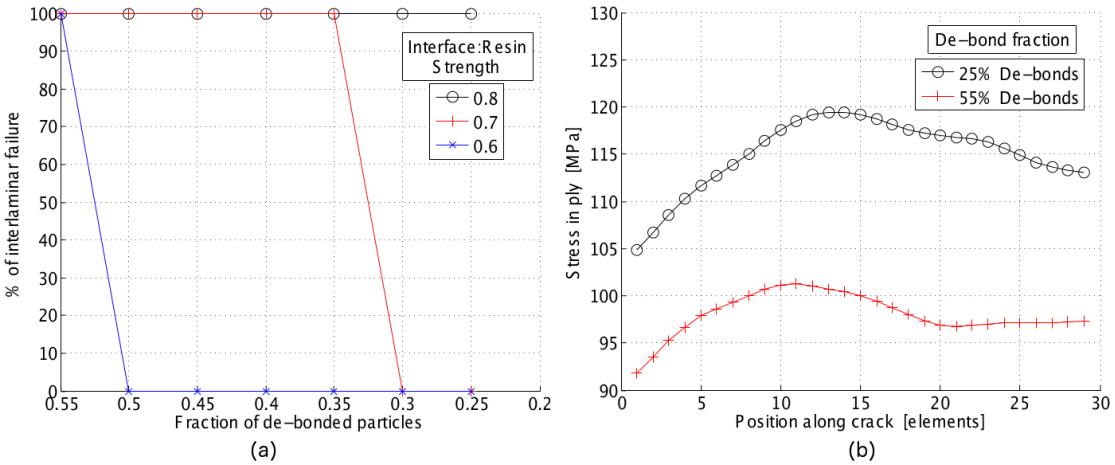

Figure 5: Graphs showing the effects of particle de-bond density on, (a) the crack path at different fibre interface strengths, and (b) the maximum in-plane principal stress in the neighbouring ply above the ROI (crack from left to right)

Figure 5(b) shows the distribution of the stresses in the neighbouring ply at and ahead of the 'crack tip'. The stress values were measured when a designated A-FEM resin element failed ahead of the starter crack, in order to compare a 'propagating' crack state. It is evident that when there are fewer particle de-bonds, the stress in the neighbouring ply is distinctly higher, which may then be expected to promote intralaminar failure. These results suggest that the key effect of the particle de-bonds is to relieve the stresses at the fibre interface by creating a more compliant interlayer and trapping the crack within it.

4.3 – Particle cohesive property effects

In reality, the process of particle de-bonding may be expected to add some toughness from the creation of new crack surfaces or bridging effects, therefore, the particles were assigned cohesive properties in this study (Model 2). This can be used to represent toughened interlayers, such as Mat. B, where the particles are drawn across the crack flanks and are likely to add a significant traction. This is seen in Figure 6(a), where the evolution of damage initiates from (i) particles fracturing from within, followed by the formation of (ii) particle bridges. There is also an example of the crack traversing the neat resin with a smooth crack between two particles at (iii). Given that thermoplastics on the whole are tougher than epoxies [1, 27], a crack path through the particles is expected to result in a higher macroscopic fracture toughness. To simulate this, the particles were given toughness values ranging from approximately equal to the neat resin, to a factor of eight tougher [28].

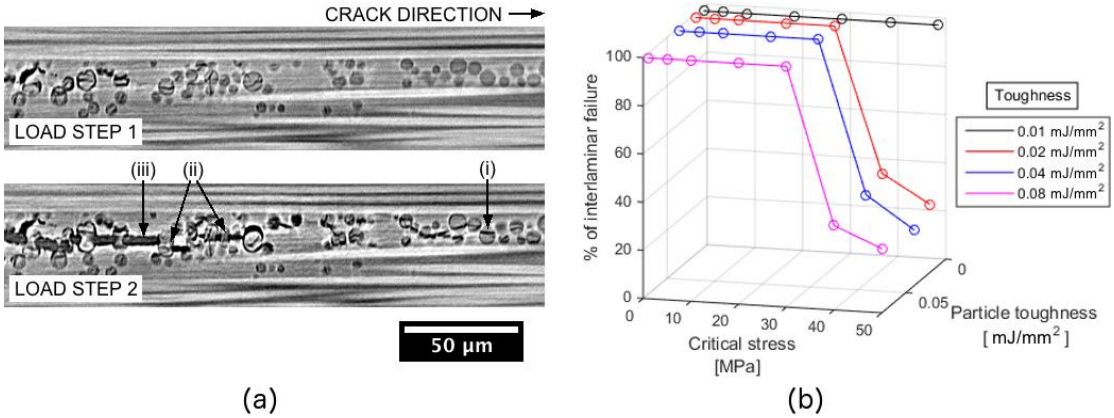

Figure 6: Showing (a) a SRCT slice of a particle-toughened region exhibiting internal particle fracture and particle bridges in Mat. B, and (b) a graph of the effects of the particle cohesive properties on the crack path

Figure 6(b) shows the effects of changing the peak strength of the particles, while maintaining a constant toughness. A linear distribution of 27 μm particles was used at a linear v_f of 50 %. The figure shows that as the peak strength of the particles increases, that the crack path will transition to the fibre interface, with this transition occurring between 30 and 40 MPa, with the exception of the 0.01 mJ/mm^2 particle toughness, where the transition occurs at 70 MPa. This difference may be due to the particle toughness being lower than the resin (0.0125 mJ/mm^2). The transition point between 30 to 40 MPa was investigated further by increasing the toughness to 0.64 mJ/mm^2, but this did not move the transition point to a lower cohesive strength than 30 MPa. This suggests that the crack path is more sensitive to changes in the strength

of the particle rather than their toughness, implying that the crack path is initiation controlled.

4.4 – Particle size and spacing effects

The following simulations maintained the linear particle v_f at 50 % whilst altering the particle sizes and consequently their spacing, as shown in Figure 3(b). The strength of the particles was also simultaneously investigated, as this was found to have a strong influence on the crack path. The particle toughness was maintained at 0.02 mJ/mm^2, and fibre interface strengths of 40 MPa and 35 MPa are presented in Figures 7 (a) and (b) respectively (Models 3 & 4)

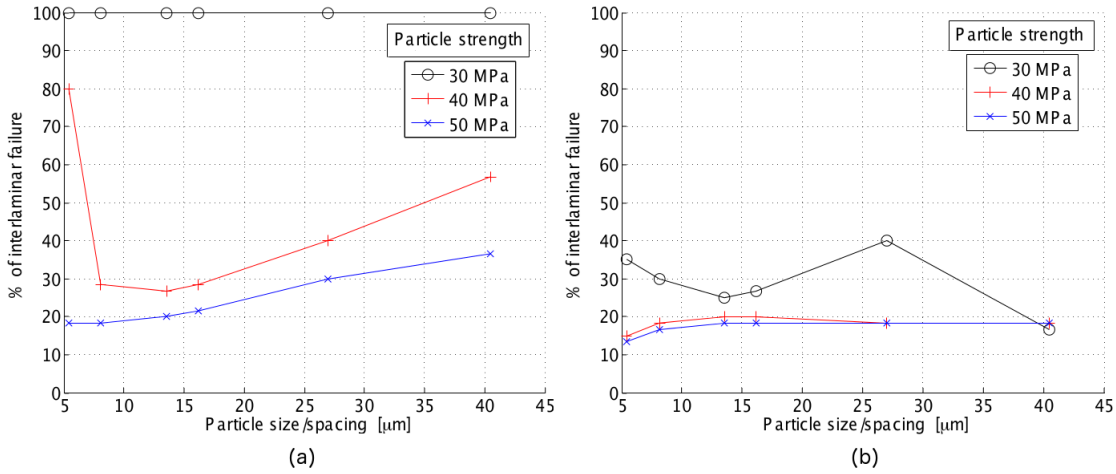

Figure 7: Particle strength, size and distribution effects on crack path with a fibre interface strength of (a) 0.8 and (b) 0.7 relative to the neat resin (constant 50 % v_f)

Figure 7(a) shows that if the strength of the particle was 30 MPa, that the crack path would follow the particles, which is consistent with Figure 6(b). However, as the particle strength increased to 40 MPa, only the smaller 5 μm particles spaced by 5 μm gaps could maintain interlaminar failure for 80 % of the ROI. As the particle size and spacing increased, there was a dip in the fraction of interlaminar failure, suggesting that smaller particles spaced closer together are more effective at maintaining interlaminar failure. This minimum was followed by an increase in the proportion of interlaminar failure, due to the crack following only the first particle in each case, after which the fibre interface failed between the first and second particles. This effect may be expressed in terms of St. Venant's principle; whereby the effect of larger particles may be experienced further towards the interface. This trend is similar to that observed at a particle strength of 50 MPa, but in this case, even the smallest and most closely spaced particles could not maintain interlaminar failure, again emphasizing the role of particle strength.

Figure 7(b) shows an overall reduction in the fraction of interlaminar failure as the fibre interface strength was reduced to 35 MPa. This is consistent with the previous findings of Figure 5(a), highlighting the role of the strength of the fibre interface relative to the resin. The results for the particle strength of 30 MPa also suggest that smaller, more closely-spaced particles are more likely to retain failure within the interlayer. However, the peak shown for a 27 μm particle may be reflecting the critical particle size/spacing (i.e. size of the particle-depleted region), at which the particle just starts to fracture before failure initiation at the interface.

4.5 – Particle spacing and proximity to ply effects

The final two simulations investigated; (a) the particle spacing (Model 5), illustrated in Figure 3(c); and (b) the particle proximity to the fibre interface (Model 6). Figure 8(a) shows that as the spacing between the particles increased, the crack path would transition to the fibre interface, corresponding to the CT observations in Figure 4(a). The different particle sizes considered show that the material containing the larger particles tolerated an increased spacing more than the material containing smaller ones. However, the increased particle v_f in the ROI must be recognised, which has been previously shown to play a large role in determining crack path (Figure 5(a)). Figure 8(b) shows the effects of the particle proximity to the fibre interface using a particle size of 24.3 μm. The plot shows that if the particles are closer to the fibre interface, the crack path is more likely to transition to this interface. It also shows that for the particles closer to the ply, that the particle spacing is also playing a role maintaining the crack path inside the interlayer since the transition occurs as the spacing is increased, consistent with Figure 8(a).

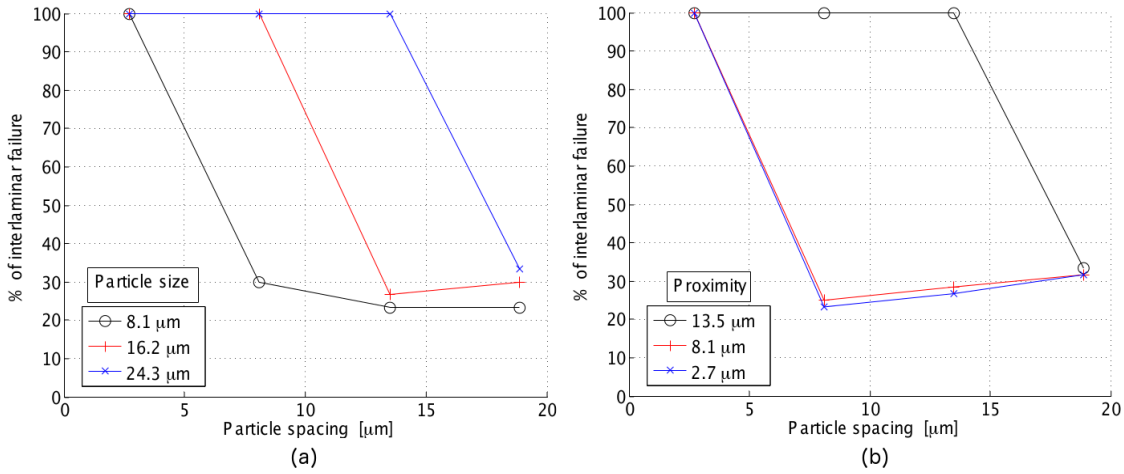

Figure 8: Graphs showing the effects of (a) particle spacing and (b) particle proximity to the ply

5 DISCUSSION

The key findings are summarised in Table 2, where the variables that influence the crack path in the models are properties that can be controlled (within certain limitations) by the manufacturer. The SRCT data and the present models show that in these material systems, the critical mechanism which determines structural performance is fibre interface failure ahead of the main crack, highlighting the competitive role of fibre-matrix strength in crack path determination, rather than the fracture mechanics of a discrete crack tip (*viz*. a given crack tip simply following the lowest energy path ahead of it) in determining behaviour. Both the models and the *in situ* experiments and CT images show that there appear to be, for a given interlayer thickness and particle size, a critical size of particle-depleted region that may result in the crack deviating to the fibre interface (Table 2, Row 1). Therefore, achieving a more uniform particle distribution appears to be mechanistically significant in reducing the proportion of particle-depleted regions and the consequent fraction of smooth, ligament-free, lower toughness crack path at the fibre interface.

At a constant v_f, the models showed that smaller, more closely spaced particles that are further away from the fibre interfaces will favour an interlaminar crack path. However, a decreasing particle v_f was shown to increase the stress in the neighbouring ply, which led to failure at the fibre interface, consistent with the simple stress-based deterministic nature of fracture within the model (Table 2, Row 2). Similarly, the model also showed that the crack path was more sensitive to the cohesive strength of the particles, rather than their toughness. The early fracture of the Mat. B particles ahead of the main crack (Figure 6(a)), and their ability to plastically deform while remaining bonded, suggests that an appropriate cohesive law would have a low initiation strength, and a large critical opening. In the models, readily fracturing particles acted to reduce the stresses at the fibre interfaces, suggesting that the internal fracture of the particles (Mat. B) or de-bonding particles (Mat. A) serve to increase the local compliance of the interlayer, moderating and redistributing crack tip stresses and therefore limiting the peak stresses experienced at the fibre interface (Table 2, Row 3). Following this, added toughness may come from the bridging processes supported by the interlayer microstructure.

Table 2: Variables identified to control crack path

Key variables	Schematic
Small, closely dispersed particles further from the fibre interfaces favoured interlaminar failure. Particle-depleted regions trigger fibre interface failure and result in a crack path along the fibres.	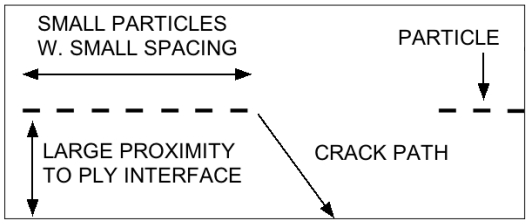
A lower particle volume fraction of readily de-bonding particles will increase the stress in the neighbouring ply. This can trigger an alternative crack path along the fibre interface or within the ply.	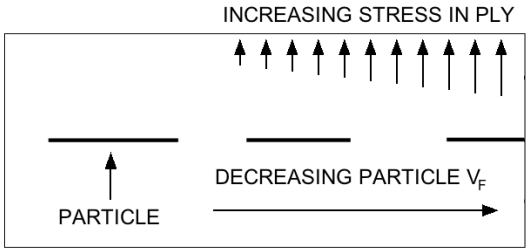
Crack path is initiation controlled, with the critical strength of competing fracture micro-mechanisms a key variable. Weak particles reduce stresses at the fibre interface above and below their location.	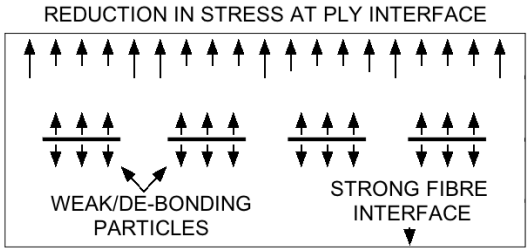

6 CONCLUSIONS

The results presented in this work offer insight regarding the mechanisms that contribute to the ability for a toughened interlayer to keep delamination cracks 'trapped' within a macroscopically high energy crack path. Several variables were shown to have an effect on the interlaminar fracture. The particle volume fraction was shown to play a large role in determining the crack path and on the stresses in the ply above the ROI, consistent with the crack path observations from CT imaging. Increased particle spacing and proximity to the ply were also shown to trigger crack migration to the fibre interface. Interestingly, the strength of the particles appeared to play a larger role than their absolute toughness, suggesting that the interlaminar crack path is initiation controlled. The concept that controlling the peak local strengths of the competing mechanisms is important was also demonstrated by a transition to the fibre interface following a reduction in its strength. The model implies that the role of the particles is to alleviate the stresses at the fibre interface by creating a more compliant interlayer, thus trapping the crack in the tougher region.

Overall, it has been shown that particle fracture or de-bonding ahead of a primary crack tip, and subsequent coalescence with the propagating main crack can be captured using A-FEM elements. The chronology of damage evolution was also captured, whereby the fibre interface failed prior to the main crack tip reaching it. It is acknowledged that a 2D model and the highly idealised representation of the particles has limitations, however, the trends identified here broadly agree with those observed experimentally via CT.

ACKNOWLEDGEMENTS

The authors acknowledge Cytec Industries Ltd. for their sponsorship and materials supply, and the technical support from Dr. Kingsley Ho. The μ-VIS centre at the University of Southampton for provision of tomographic imaging facilities, supported by EPSRC grant EP-H01506X, and the support from Dr. Richard Boardman and Dr. Neil (?) O'Brien. The support from researchers Derek Schesser and Bao-Chan Do from the Univeristy of Miami. The authors also acknowledge support from Dr. ____ ? Modregger at the Swiss Light Source and funding from the Community's Seventh Framework Programme (FP7/2007-2013) under grant agreement n.°312284 (for CALIPSO).

REFERENCES

[1] M. O. W. Richardson, M. J. Wisheart, Review of low-velocity impact properties of composite materials, Compos. Part A. 27 (1996) 1123–1131.

[2] N. Odagiri, T. Muraki, K. Tobukuro, Toughness Improved High Performance Torayca Prepreg T800H/3900 Series, 33rd International SAMPE Symposium, (1988) 272-283.

[3] N. Odagiri, H. Kishi, M. Yamashita, Development of TORAYCA prepreg P2302 carbon fiber reinforced plastic for aircraft primary structural materials, Adv. Compos. Mater. 5 (1996) 249-52.

[4] M. Yasaee, I. P. Bond, R. S. Trask, E. S. Greenhalgh, Mode II interfacial toughening through discontinuous interleaves for damage suppression and control, Compos. Part A Appl. Sci. Manuf. 43 (1) (2012) 121–128.

[5] M. Yasaee, I. P. Bond, R. S. Trask, E. S. Greenhalgh, Mode I interfacial toughening through discontinuous interleaves for damage suppression and control, Compos. Part A Appl. Sci. Manuf. 43 (1) (2012) 198–207.
[6] S. Singh, I. K. Partridge, Mixed-Mode Fracture in an Interleaved Carbon-Fibre/Epoxy Composite, Compos. Sci. Technol. 55 (1996) 319–327.
[7] S.-Y. Fu, X.-Q. Feng, B. Lauke, Y.-W. Mai, Effects of particle size, particle/matrix interface adhesion and particle loading on mechanical properties of particulate–polymer composites, Compos. Part B Eng. 39 (6) (2008) 933–961.
[8] M. Zamanian, M. Mortezaei, B. Salehnia, J. E. Jam, Fracture toughness of epoxy polymer modified with nanosilica particles: Particle size effect, Eng. Fract. Mech. 97 (2013) 193–206.
[9] A. G. Evans, Z. B. Ahmad, D. G. Gilbert, P. W. R. Beaumont, Mechanisms of toughening in rubber toughened polymers, Acta Met. 34 (1) (1986) 79–87.
[10] Y. Huang, A. J. Kinloch, The sequence of initiation of the toughening micromechanisms in rubber-modified epoxy polymers, Polymers (Basel). 33 (24) (1992) 5338–5340.
[11] Y. Huang, A. J. Kinloch, Modelling of the toughening mechanisms in rubber-modified epoxy polymers Part II: A quantitative description of the microstructure-fracture, J. Mater. Sci. 27 (1992) 2763–2769.
[12] W.L. Bradley, Relationship of matrix toughness to interlaminar fracture toughness, In: Friedrich K, editor. Application of fracture mechanics to composite materials. Amsterdam: Elsevier (1989) 159-87.
[13] M. R. Groleau, Y. Shi, A. F. Yee, J. L. Bertram, H. J. Sueb, P. C. Yang, Mode II Fracture of Composites Interlayered with Nylon Particles, Compos. Sci. Technol. 56 (1996) 1223–1240.
[14] M. Hojo, S. Matsuda, M. Tanaka, S. Ochiai, A. Murakami, Mode I delamination fatigue properties of interlayer-toughened CF/epoxy laminates, Compos. Sci. Technol. 66 (5) (2006) 665-675.
[15] D. J. Bull, A. E. Scott, S. M. Spearing, I. Sinclair, The influence of toughening-particles in CFRPs on low velocity impact damage resistance performance, Compos. Part A Appl. Sci. Manuf. 58 (2014) 47–55.
[16] G. Borstnar, M. N. Mavrogordato, L. Helfen, I. Sinclair, S. M. Spearing, Interlaminar fracture micro-mechanisms in toughened carbon fibre reinforced plastics investigated via synchrotron radiation computed tomography and laminography, Compos. Part A Appl. Sci. Manuf. 71 (2015) 176–183.
[17] H.-M. Hsiao, C.-N. Ni, M.-D. Wu, C.-W. Lin, A novel optical technique for observation of global particle distribution in toughened composites, Compos. Part A Appl. Sci. Manuf. 43 (9) (2012) 1523–1529.
[18] W. Liu, Q. D. Yang, S. Mohammadizadeh, X. Y. Su, An efficient augmented finite element method for arbitrary cracking and crack interaction in solids, Int. J. Numer. Methods Eng. 99 (2014) 438–468.
[19] Y. C. Gu, J. Jung, Q. D. Yang, W. Q. Chen, An Inertia-Based Stabilizing Method for Quasi-static Simulation of Unstable Crack Initiation and Propagation, J. Appl. Mech. 82 (10) (2015) 101010-101010-12.
[20] I. Babuska, J. M. Melenk, The partition of unity method, Int. J. Numer. Methods Eng. 40 (1997) 727–758.
[21] F. P. van der Meer, L. J. Sluys, Mesh-independent modeling of both distributed and discrete matrix cracking in interaction with delamination in composites, Eng. Fract. Mech. 77 (4) (2010) 719–735.

[22] X. J. Fang, Z. Q. Zhou, B. N. Cox, Q. D. Yang, High-fidelity simulations of multiple fracture processes in a laminated composite in tension, J. Mech. Phys. Solids. 59 (7) (2011) 1355–1373.
[23] K. Matous, M.G. Kulkarni, P.H. Geubelle, Multiscale cohesive failure modeling of heterogeneous adhesives, J. Mech. Phys. Solids 56 (2008) 1511-1533.
[24] P. Cloetens, M. Pateyron-Salomé, J. Y. Buffière, G. Peix, J. Baruchel, F. Peyrin, M. Schlenker, Observation of microstructure and damage in materials by phase sensitive radiography and tomography, J. Appl. Phys. 81 (9) (1997) 5878 -5886.
[25] F. Marone, M. Stampanoni, GRIDREC software, J. Synchrotron Rad. 19 (2012) 1029–1037.
[26] Q. Yang, B. Cox, Cohesive models for damage evolution in laminated composites, Int. J. Fract. 133 (2) (2005) 107–137.
[27] F. Touchard-Lagattu, M. C. Lafarie-Frenot, Damage and inelastic deformation mechanisms in notched thermoset and thermoplastic laminates, Compos. Sci. Technol. 56 (5) (1996) 557–568.
[28] A. C. Garg, Failure Mechanisms in Toughened Epoxy Resins Review A, Compos. Sci. Technol. 31 (1988) 179–223.